Simultaneous exoplanet detection and instrument aberration retrieval in multispectral coronagraphic imaging

M. Ygouf,[1,2*] L. M. Mugnier,[1] D. Mouillet,[2] T. Fusco,[1] J.-L. Beuzit[2]

[1] *ONERA - The French Aerospace Lab*
F-92322 Châtillon, France
[2] *UJF-Grenoble 1 / CNRS-INSU, Institut de Planétologie et d'Astrophysique de Grenoble (IPAG) UMR 5274,*
Grenoble, F-38041, France
**marie.ygouf@onera.fr*

Abstract: High contrast imaging for the detection and characterization of exoplanets rests upon the instrument's capability to cancel the light of the host star. Some current post-processing methods for calibrating out the residual speckles use information redundancy offered by multispectral imaging but do not use any prior information on the origin of these speckles. We develop, in a Bayesian framework, an inversion method that is based on an analytical imaging model in order to estimate both the speckles and the object map. The model links the instrumental aberrations to the speckle pattern in the image focal plane, distinguishing between aberrations upstream and downstream of the coronagraph. We propose and validate several numerical techniques to handle the difficult minimization issues of *phase retrieval* and achieve a contrast of 10^6 at 0.2 arcsec from simulated images, in presence of photon noise. This opens up the tests on real data where the ultimate performance may override the current techniques if the instrument has good and stable coronagraphic imaging quality. This pave the way for new astrophysical exploitations or even to new designs for the future instruments.

OCIS codes: 100.3020, 100.3190, 100.4145, 100.5070, 110.4234, 110.6770

References and links

1. G. Chauvin, A.-M. Lagrange, C. Dumas, B. Zuckerman, D. Mouillet, I. Song, J.-L. Beuzit, and P. Lowrance, "A giant planet candidate near a young brown dwarf. Direct VLT/NACO observations using IR wavefront sensing," Astron. Astrophys. **425**, L29–L32 (2004).
2. A.-M. Lagrange, M. Bonnefoy, G. Chauvin, D. Apai, D. Ehrenreich, A. Boccaletti, D. Gratadour, D. Rouan, D. Mouillet, S. Lacour, and M. Kasper, "A Giant Planet Imaged in the Disk of the Young Star β Pictoris," Science **329**, 57– (2010).
3. C. Marois, B. Macintosh, T. Barman, B. Zuckerman, I. Song, J. Patience, D. Lafrenière, and R. Doyon, "Direct Imaging of Multiple Planets Orbiting the Star HR 8799," Science **322**, 1348– (2008).
4. P. Kalas, J. R. Graham, E. Chiang, M. P. Fitzgerald, M. Clampin, E. S. Kite, K. Stapelfeldt, C. Marois, and J. Krist, "Optical Images of an Exosolar Planet 25 Light-Years from Earth," Science **322**, 1345– (2008).
5. J. R. Graham, B. Macintosh, R. Doyon, D. Gavel, J. Larkin, M. Levine, B. Oppenheimer, D. Palmer, L. Saddlemyer, A. Sivaramakrishnan, J. Veran, and K. Wallace, "Ground-Based Direct Detection of Exoplanets with the Gemini Planet Imager (GPI)," ArXiv e-prints (2007).
6. S. Hinkley, B. R. Oppenheimer, N. Zimmerman, D. Brenner, I. R. Parry, J. R. Crepp, G. Vasisht, E. Ligon, D. King, R. Soummer, A. Sivaramakrishnan, C. Beichman, M. Shao, L. C. Roberts, A. Bouchez, R. Dekany,

L. Pueyo, J. E. Roberts, T. Lockhart, C. Zhai, C. Shelton, and R. Burruss, "A New High Contrast Imaging Program at Palomar Observatory," Pub. Astron. Soc. Pacific **123**, 74–86 (2011).
7. F. Martinache and O. Guyon, "The Subaru Coronagraphic Extreme-AO Project," in "Society of Photo-Optical Instrumentation Engineers (SPIE) Conference Series," (2009).
8. J.-L. Beuzit, M. Feldt, K. Dohlen, D. Mouillet, P. Puget, F. Wildi, L. Abe, J. Antichi, A. Baruffolo, P. Baudoz, A. Boccaletti, M. Carbillet, J. Charton, R. Claudi, M. Downing, C. Fabron, P. Feautrier, E. Fedrigo, T. Fusco, J.-L. Gach, R. Gratton, T. Henning, N. Hubin, F. Joos, M. Kasper, M. Langlois, R. Lenzen, C. Moutou, A. Pavlov, C. Petit, J. Pragt, P. Rabou, F. Rigal, R. Roelfsema, G. Rousset, M. Saisse, H.-M. Schmid, E. Stadler, C. Thalmann, M. Turatto, S. Udry, F. Vakili, and R. Waters, "SPHERE: a planet finder instrument for the VLT," in "Society of Photo-Optical Instrumentation Engineers (SPIE) Conference Series," (2008).
9. M. E. Kasper, J. Beuzit, C. Verinaud, N. Yaitskova, P. Baudoz, A. Boccaletti, R. G. Gratton, N. Hubin, F. Kerber, R. Roelfsema, H. M. Schmid, N. A. Thatte, K. Dohlen, M. Feldt, L. Venema, and S. Wolf, "EPICS: the exoplanet imager for the E-ELT," in "Society of Photo-Optical Instrumentation Engineers (SPIE) Conference Series," (2008).
10. R. Racine, G. A. Walker, D. Nadeau, and C. Marois, "Speckle noise and the detection of faint companions," Pub. Astron. Soc. Pacific **112**, 587–594 (1999).
11. C. Marois, R. Doyon, R. Racine, and D. Nadeau, "Efficient Speckle Noise Attenuation in Faint Companion Imaging," Pub. Astron. Soc. Pacific **112**, 91–96 (2000).
12. W. B. Sparks and H. C. Ford, "Imaging Spectroscopy for Extrasolar Planet Detection," Astrophys. J. **578**, 543–564 (2002).
13. N. Thatte, R. Abuter, M. Tecza, E. L. Nielsen, F. J. Clarke, and L. M. Close, "Very high contrast integral field spectroscopy of ab doradus c: 9-mag contrast at 0.2arcsec without a coronagraph using spectral deconvolution," Mon. Not. R. Astron. Soc. **378**, 1229–1236 (2007).
14. D. Lafrenière, C. Marois, R. Doyon, D. Nadeau, and É. Artigau, "A New Algorithm for Point-Spread Function Subtraction in High-Contrast Imaging: A Demonstration with Angular Differential Imaging," Astrophys. J. **660**, 770–780 (2007).
15. J. R. Crepp, L. Pueyo, D. Brenner, B. R. Oppenheimer, N. Zimmerman, S. Hinkley, I. Parry, D. King, G. Vasisht, C. Beichman, L. Hillenbrand, R. Dekany, M. Shao, R. Burruss, L. C. Roberts, A. Bouchez, J. Roberts, and R. Soummer, "Speckle Suppression with the Project 1640 Integral Field Spectrograph," Astrophys. J. **729**, 132–+ (2011).
16. D. Burke and N. Devaney, "Enhanced faint companion photometry and astrometry using wavelength diversity," Journal of the Optical Society of America A **27**, A260000 (2010).
17. R. A. Gonsalves, "Phase retrieval and diversity in adaptive optics," Optical Engineering **21**, 829–832 (1982).
18. R. G. Paxman and J. H. Seldin, "Fine-resolution astronomical imaging with phase-diverse speckle," in "Society of Photo-Optical Instrumentation Engineers (SPIE) Conference Series," , P. S. Idell, ed. (1993), pp. 287–298.
19. J.-F. Sauvage, L. Mugnier, G. Rousset, and T. Fusco, "Analytical expression of long-exposure AO-corrected coronagraphic image. First application to exoplanet detection," J. Opt. Soc. Am. A (2010).
20. M. D. Perrin, A. Sivaramakrishnan, R. B. Makidon, B. R. Oppenheimer, and J. R. Graham, "The Structure of High Strehl Ratio Point-Spread Functions," Astrophys. J. **596**, 702–712 (2003).
21. C. Cavarroc, A. Boccaletti, P. Baudoz, T. Fusco, and D. Rouan, "Fundamental limitations on Earth-like planet detection with extremely large telescopes," Astron. Astrophys. **447**, 397–403 (2006).
22. R. Soummer, A. Ferrari, C. Aime, and L. Jolissaint, "Speckle Noise and Dynamic Range in Coronagraphic Images," Astrophys. J. **669**, 642–656 (2007).
23. M. Ygouf, L. Mugnier, J.-F. Sauvage, T. Fusco, D. Mouillet, and J.-L. Beuzit, "Approximate analytical model of AO-corrected coronagraphic imaging, with a view to exoplanet detection and characterisation," in "In the Spirit of Lyot 2010," (2010).
24. J.-P. Véran, F. Rigaut, H. Matre, and D. Rouan, "Estimation of the adaptive optics long exposure point spread function using control loop data," J. Opt. Soc. Am. A **14**, 3057–3069 (1997).
25. L. M. Mugnier, T. Fusco, and J.-M. Conan, "MISTRAL: a myopic edge-preserving image restoration method, with application to astronomical adaptive-optics-corrected long-exposure images," Journal of the Optical Society of America A **21**, 1841–1854 (2004).
26. S. Meimon, L. M. Mugnier, and G. Le Besnerais, "Self-calibration approach for optical long-baseline interferometry imaging," Journal of the Optical Society of America A **26**, 108–+ (2008).
27. E. Thiébaut and L. Mugnier, "Maximum a posteriori planet detection and characterization with a nulling interferometer," in "IAU Colloq. 200: Direct Imaging of Exoplanets: Science & Techniques," , C. Aime & F. Vakili, ed. (2006), pp. 547–552.
28. A. Blanc, "Identification de réponse impulsionnelle et restauration d'images : apports de la diversité de phase," Ph.D. thesis, Université Paris XI Orsay (2002).
29. L. M. Mugnier, A. Blanc, and J. Idier, "Phase diversity: a technique for wave-front sensing and for diffraction-limited imaging," in "Advances in Imaging and Electron Physics," , vol. 141, P. Hawkes, ed. (Elsevier, 2006), chap. 1, pp. 1–76.
30. E. Thiebaut, "Optimization issues in blind deconvolution algorithms," in "Society of Photo-Optical Instrumenta-

tion Engineers (SPIE) Conference Series," , J.-L. Starck & F. D. Murtagh, ed. (2002), pp. 174–183.
31. A. Cornia, "High-contrast differential image processing for extrasolar planet detection," Ph.D. thesis, École Doctorale d'Astronomie et d'Astrophysique d'Île de France (2010).
32. A. Cornia, L. M. Mugnier, D. Mouillet, A. Vigan, A. Eggenberger, G. Rousset, A. Boccaletti, M. Carbillet, K. Dohlen, T. Fusco, J. Carson, and G. Montagnier, "Optimal method for exoplanet detection by spectral and angular differential imaging," in "Adaptive Optics Systems II," , vol. 7736, B. L. Ellerbroek, M. Hart, N. Hubin, and P. L. Wizinowich, eds. (Proc. Soc. Photo-Opt. Instrum. Eng., 2010), vol. 7736, p. 7736 1E.
33. A. Boccaletti, P. Riaud, and D. Rouan, "Speckle Symmetry with High-Contrast Coronagraphs," pasp **114**, 132–136 (2002).

1. Introduction

Ground-based instruments have now demonstrated the capability to detect planetary mass companions [1, 2, 3, 4] around bright host stars. By combining an adaptive optics (AO) system and coronagraphs, some first direct detections from the ground have been possible in favorable cases, at large separations and in young systems when low mass companions are still warm ($\geq 1000\,\mathrm{K}$) and therefore not too faint. There is a very strong astrophysical case to improve the high contrast detection capability (10^5 for a young giant planet to 10^{10} for an earth-like planet in the near infrared) very close to stars (< 0.1" to 1").

Several instruments will be capable of performing multispectral imaging and will allow characterizing the planets by measuring their spectra. It is the case of GPI (Gemini) [5], Palm 3000 (Palomar) [6], SCExAO (Subaru) [7], SPHERE (VLT) [8] and several others that will follow such as EPICS (E-ELT) [9]. By combining an extreme adaptive optics (Ex-AO) and more accurate coronagraphs than before, the level of star light cancellation is highly improved, leading to a better signal to noise ratio. Yet, the residual host star light is affected by the instrument aberrations to form a pattern of intensity variations or "speckle noise" on the final image. Part of the speckles cannot be calibrated as they evolve on various time scales (neither fast enough to smooth down a halo nor stable enough) and for this reason, these "quasi-static speckles" are one of the main limitations for high contrast imaging.

A number of authors have discussed the challenge posed by the elimination of speckle noise in high contrast multispectral images. It can be done by post-processing, after the best possible observations. As images are highly spectrally correlated, one can use the wavelength dependance of the speckles to subtract them. In the particular case of coronagraphic multispectral imaging, only some empirical methods have been developed to subtract the speckle field from the image in the focal plane.

We propose an alternative approach based on a parametrized imaging model for the post-processing of multispectral coronagraphic imaging corrected by an extreme adaptive optic system in the near-infrared domain. The aberrations and bright companions at small separations are estimated jointly in a bayesian framework. Particularly, it is possible to take advantage of prior information such as an accurate knowledge on the aberration levels. This kind of approach will be increasingly efficient for the instruments getting closer to the ideal case of low aberrations and high efficiency coronagraphs.

In section 2, we explain how previous methods use the information redundancy for the speckle suppression in high contrast imaging. Then, we describe the advantages of a joint bayesian estimation of the aberrations in the pupil plane and the planet map, based on a parametrized model of coronagraphic imaging. Section 3 presents the long exposure coronagraphic imaging model which is used to simulate the images and restore them. The case of an approximate model is also studied. Section 4 describes respectively theoretical and numerical issues of an alternating restoration algorithm. Particularly, the aberration estimation presents minimization difficulties to which we bring some solutions. In section 5, our image post-processing is validated by restoring images simulated with a perfect coronagraph.

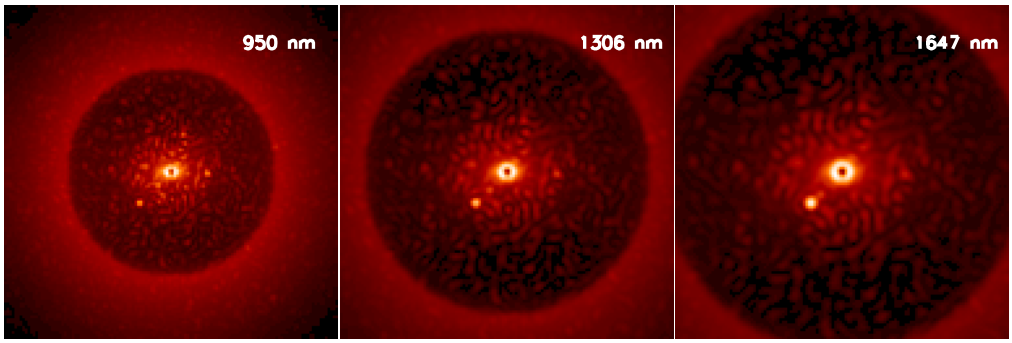

Fig. 1. Evolution of the speckle field with the wavelength. Simulated images at 950, 1306 and 1647 nm for a 10^3 star flux over planet flux contrast. The dynamic is adapted to the visualization. The speckle field moves with the wavelength but not the planet position.

2. Post-processing speckles subtraction and multispectral imaging

Several empirical post-processing methods have already been proposed in order to overcome the problem of detection limitation caused by the "quasi-static speckles". Some of these methods use the wavelength dependence of the speckle pattern (Fig. 1) to estimate it and subtract it from the image, while preserving both the flux and spectrum of the planet.

Racine et al. (1999) suggested to subtract two images at different wavelengths to eliminate both the point-spread function (PSF) and the speckle field in non-coronagraphic images [10]. The main limitation of this *simultaneous differential imaging* (SDI) method comes from the residuals caused by the evolution of the general PSF profile and of the speckle pattern with wavelength. These residuals can be reduced by increasing the number of images used for the speckle field subtraction. Marois et al. (2000) showed with their *double difference* method that adding another image to the *SDI* improves the signal to noise ratio in the final image of the restored companion [11]. The case of multispectral images has been tackled by Sparks and Ford (2002) who described the so-called *spectral deconvolution* method in the framework of space-based observations for an instrument combining a coronagraph and an integral-field spectrometer (IFS) [12]. The method, later improved by Thatte et al. [13], is entirely based on a speckle intensity fit by low-order polynomials as a function of wavelength, in the focal plane. More recently, Crepp et al. (2011) combined this method with the LOCI algorithm which is based on linear combination of images [14] and restored on-sky images from the Projet 1640 IFS on the Palomar telescope [15]. These methods are applicable to any optical system and in particular to those with coronagraphs. But preserving the planet signals from being eliminated with the speckles is challenging because the planet presence is not explicitly modeled.

Besides, some information on the measurement system can be very useful to disentangle a planet from the speckle field. Burke et al. (2010) combined classical empirical techniques of differential imaging with a multi-wavelength *phase retrieval* method to estimate the aberration pattern in the pupil plane with a simple imaging model without a coronagraph [16]. This multi-wavelength *phase retrieval* is nicknamed "wavelength diversity" [17] because it uses different images at different wavelengths to bring information diversity as one would do with, e.g., defocus in *phase diversity* [17, 18]. But contrary to the *phase diversity*, the "wavelength diversity" does not remove the phase sign ambiguity. The inversion algorithm is based on a maximum-likelihood estimator, which measures the discrepancy between the data and an imaging model. The minimization of this estimator is all the more difficult as the number of unknowns to esti-

mate is high. This issue is overcome by the parcimonial parametrization of the unknown phases ϕ_λ through the optical-path-errors (or aberrations) δ, assuming that the former are achromatic: $\phi(\lambda) = 2\pi\delta/\lambda$. This allows one to exploit jointly the images at all wavelengths to estimate efficiently the aberrations: the map of the unknown optical-path-errors δ is in common to all wavelengths. The number of unknowns is thus limited and the problem constrained. In the present case, Burke's wavelength diversity method does not apply readily, as it assumes non coronagraphic imaging, whereas we consider the highly non-linear case of a coronagraphic imaging model.

That is why we propose to take advantage of a combined use of wavelength diversity and a Bayesian inversion to jointly estimate the aberrations in the pupil plane and the planet map. The joint estimation aims at taking up the challenge of preserving the planets signal. An advantage of the Bayesian inversion is that it can potentially include an important regularization diversity to constrain the problem, using for example prior information on the noise, the planet map (position, spectrum, ...) or the aberrations. In the Bayesian framework, the criterion to be minimized is the sum of two terms: the data fidelity term, which measures the distance between the data and the imaging model, and one or some penalty terms. An important difficulty is to define a realistic coronagraphic imaging model which depends on parameters (aberrations...) that can be either calibrated beforehand or estimated from the data.

3. Parametric model of multi-spectral coronagraphic imaging

In order to carry out the Bayesian inversion, we need a parametric direct model of coronagraphic imaging. This direct model will also be useful to simulate our test images.

We consider a non linear existing expression [19] and try to simplify it to be used in an inversion algorithm. We assume that the coronagraph is "perfect" in the sense defined in [19] ; essentially, we mean that the coherent energy is perfectly canceled out. The aberrations, or optical-path-errors, δ are assumed to be achromatic which is a reasonable assumption in the envisaged wavelength band: 950 to 1650 nm. The variable $\alpha \equiv (\alpha_x, \alpha_y)$ represents the angular positions in the focal plane in radians and the variable $\rho \equiv (\rho_x, \rho_y)$ is the angular position in the pupil plane in radians^{-1}. Finally, $\lambda\rho \equiv (\lambda\rho_x, \lambda\rho_y)$ corresponds to the spatial position in the pupil plane in meters.

3.1. Global imaging model

We assume that, for an AO-corrected coronagraphic image at the wavelength λ, the direct model is the following sum of three terms, separating the residual coronagraphic stellar halo, the circumstellar source (for which the impact of coronagraph is neglected) and noise n_λ:

$$i_\lambda(\alpha) = f_\lambda^* \cdot h_\lambda^c(\alpha) + \left[o_\lambda \star h_\lambda^{nc}\right](\alpha) + n_\lambda(\alpha), \tag{1}$$

where the data are: $i_\lambda(\alpha)$, the image we have access to, f_λ^* is the star flux and $h_\lambda^{nc}(\alpha)$, the non-coronagraphic point spread function (PSF) which can be estimated separately. Solving the inverse problem is finding the unknowns: the object $o_\lambda(\alpha)$ and the speckle field $h_\lambda^c(\alpha)$ which we also call the "coronagraphic PSF".

3.2. Long exposure "coronagraphic PSF" model

A model description of $h_\lambda^c(\alpha)$ directly depends on the turbulence residuals and optical wave front errors. After previous works to model non coronagraphic PSFs [20] and coronagraphic PSFs [21, 22], Sauvage et al. (2010) proposed an analytical expression for coronagraphic image with a distinction between upstream and downstream aberrations [19] (cf. Appendix B). The considered optical system is composed of a telescope, a perfect coronagraph and a detector

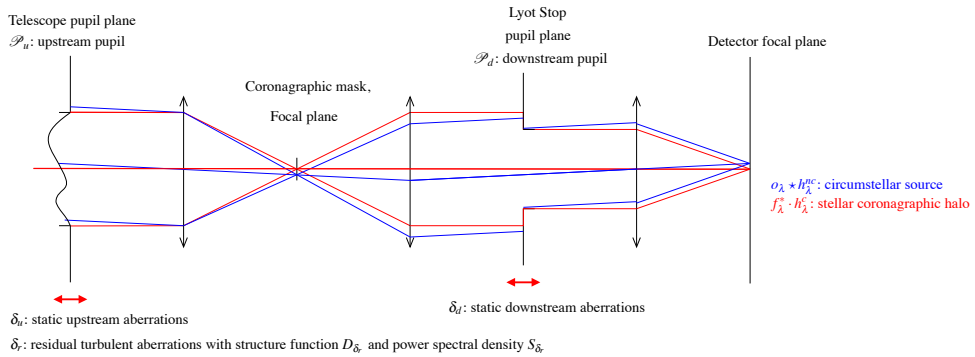

Fig. 2. Optical scheme of a coronagraphic imager. The upstream and downstream static aberrations, as well as the adopted notations are denoted δ_u and δ_d respectively. $\mathscr{A}_i(\alpha)$ denote focal plane complex amplitudes, whereas $\Psi_i(\rho)$ denote pupil plane amplitudes.

plane (cf. Figure (2)). Some residual turbulent aberrations $\delta_r(\rho,t)$ are introduced in the telescope pupil plane. $\delta_r(\rho,t)$ is assumed to be temporally zero-mean, stationary, ergodic. Because we consider only long exposure time with respect to turbulence timescales, these turbulent aberrations contribute only through their spatial statistical properties: power spectral density $S_{\delta_r}(\alpha)$ or structure function D_{ϕ_r}. The static aberrations are separated into two contributions: the aberrations upstream of the coronagraph $\delta_u(\rho)$, in the telescope pupil plane $\mathscr{P}_u(\rho)$ and the aberrations downstream of the coronagraph $\delta_d(\rho)$ in the Lyot Stop pupil plane $\mathscr{P}_d(\rho)$. The perfect coronagraph is defined as an optical device that subtracts a centered Airy pattern of maximal energy to the electromagnetic field. Finally, the "coronagraphic PSF" depends on three parameters which define our system : the aberrations maps δ_u, δ_d and D_{ϕ_r}.

3.2.1. Derivation of an approximate long exposure "coronagraphic PSF" model

As the analytical expression of h_λ^c is a highly non-linear function of the aberrations (see [19] for more details), we derived and studied the relevance of an approximate expression of this model [23]. Several works have been done to derive some approximate coronagraphic imaging models. Cavarroc et al. [21] have developed a short-exposure expression and showed by simulations that the main limitation comes from the static aberrations and particularly the aberrations upstream of the coronagraph. Here, we consider a long exposure imaging model and confirm analytically the dominance of the upstream aberrations. Soummer et al. [22] have developed a two-term expression with one static term and one turbulent term. Nevertheless, these terms are not explicitly linked to the aberrations which we are interested in.

Assuming that all the phases are small and that the spatial mean of $\phi_u(\rho)$ and $\phi_d(\rho)$ are equal to zero on the aperture, we derive a second-order Taylor expansion of expression 24 of [19]:

$$\begin{aligned}\left[h_\lambda^c\right]^{app}(\alpha) &= \left(\frac{2\pi}{\lambda}\right)^2 \left\{ \left| \widetilde{\mathscr{P}_d(\lambda\rho)} \star \widetilde{\delta_u(\lambda\rho)} \right|^2 \right\} \\ &+ \left(\frac{2\pi}{\lambda}\right)^2 \left\{ \left| \widetilde{\mathscr{P}_d(\lambda\rho)} \right|^2 \star S_{\delta_r}(\alpha) - \left\langle \left| P\left[\delta_r(\lambda\rho,t)\right] \right|^2 \right\rangle_t \cdot \left| \widetilde{\mathscr{P}_d(\lambda\rho)} \right|^2 \right\} \\ &+ o\left(\delta^2\right), \end{aligned} \tag{2}$$

where $\widetilde{\mathscr{P}_d(\lambda\rho)}$ and $\widetilde{\delta_u(\lambda\rho)}$ are the Fourier transforms of the downstream pupil and upstream aberrations respectively and $P\left[\delta_r(\lambda\rho,t)\right]$ denotes the piston of the aberration map $\delta_r(\lambda\rho,t)$.

$\left\{ \left\langle |P[\delta_r(\lambda\rho,t)]|^2 \right\rangle_t \cdot \left| \widetilde{\mathscr{P}_d(\lambda\rho)} \right|^2 \right\}$ is a corrective term that compensates for the fact that $\delta_r(\lambda\rho,t)$ is stationary and thus non-piston-free on the aperture at every instant. Note that $\left| \widetilde{\mathscr{P}_d(\lambda\rho)} \right|^2$ is the Airy pattern formed by the pupil $\mathscr{P}_d(\lambda\rho)$.

This approximate expression brings physical insight to the Sauvage et al. expression:

- The speckle patterns scales radially in λ and evolves in $1/\lambda^2$ in intensity in the data cube. It is consistent with the analysis of Sparks and Ford [12], who perform fits of low-order polynomials as a function of the wavelength after rescaling radially.
- The approximate expression can be separated into one static term and one turbulent term. This is consistent with the analysis of Soummer et al. [22] with the advantage that these terms depend on the parameters of interest. The turbulent term is simply the turbulent aberration power spectral density, as seen at the resolution of the instrument, i.e., convolved by the output pupil Airy pattern. The static term is directly function of the upstream aberrations.
- The downstream aberrations do not appear in the static term. This confirms that the role of the aberrations upstream and downstream of the coronagraph is very different and that upstream aberrations are dominant in the final image.
- Four equivalent upstream aberration sets: $\delta_u(\rho)$, $\delta_u(-\rho)$, $-\delta_u(\rho)$ and $-\delta_u(-\rho)$, that we call "quasi-equivalent" aberration maps in the following, lead to the same image (cf. Appendix A). This item is further discussed in section 4.3.3.
- By using this approximate expression for h^c_λ in the imaging model (1), we can see that there is a degeneracy between the value of the star flux and the rms value of the aberration map, if there is no turbulence. Indeed, without turbulent aberrations, the approximate model multiplied by the star flux can be written as:

$$f^*_\lambda \cdot h^c_\lambda(\delta_u) = f^*_\lambda \cdot \frac{(2\pi)^2}{\lambda^2} \cdot \left| \widetilde{\mathscr{P}_d} \star \widetilde{\delta_u} \right|^2 \tag{3}$$

  This item is further discussed in section 4.3.2.

Discussion The differences on the final image between the two models are not negligible as we can see the circularly averaged profiles of the Figure 3. Because of the Sauvage et al. expression complexity, we first thought about using the approximate model in our inversion algorithm to decrease the number of unknowns to estimate and to simplify the criterion to minimize. But a study of this approximate model [23] showed that the image simulated with the approximate model is too different from the one simulated with the Sauvage et al. expression: the computation of the root mean square of the difference between the two images leads to an error of 29%. Consequently, even if using the approximate model would considerably decrease the non-convexity of the criterion, it would probably not lead to sufficiently good results. Nevertheless, and we will discuss this in Section 4, this approximate model will be useful to improve the convergence of our criterion minimization, which is a highly critical point.

3.2.2. Assumptions on the long exposure "coronagraphic PSF" model

The information we get from the approximate model study helps us define some key assumptions for the success of the speckle field estimation with the Sauvage et al.'s long exposure "coronagraphic PSF" model.

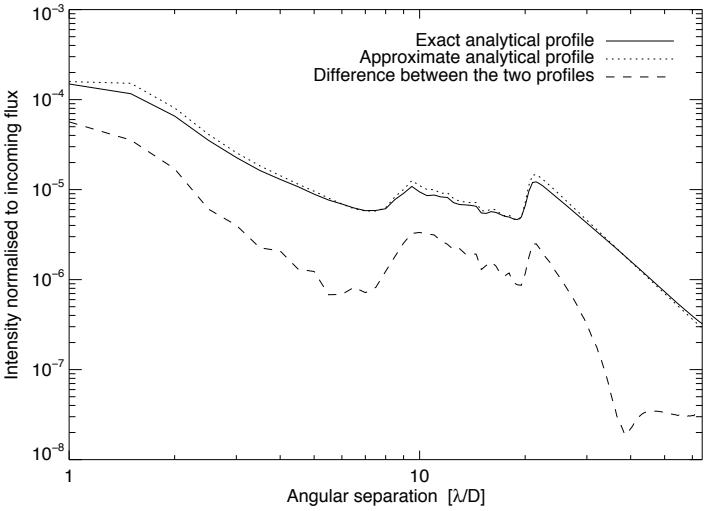

Fig. 3. Circularly averaged profiles of simulated images. Sauvage et al.'s analytical model versus Taylor expansion and error between the two models.

As they have a quite different impact on the final image, it is important to distinguish the aberrations upstream and downstream of the coronagraph. The downstream aberrations effect is lower than that of the upstream aberrations and furthermore, in foreseen systems, they are expected to be much more stable and easier to calibrate than upstream aberrations. Besides, as we consider long exposure images, the residual turbulent aberrations will be averaged to form a smooth halo easily distinguishable from a planet. Furthermore, the statistical quantity D_{ϕ_r} which characterizes this halo, will be measured through the adaptive optics system wavefront sensor [24]. Thus, in this paper, we assume that both the static downstream aberrations and the residual turbulent aberrations are calibrated and known. This decreases the number of unknowns as the only aberration map to estimate in order to get access to the "coronagraphic PSF" is the quasi-static upstream aberrations. We shall thus denote the long exposure "coronagraphic PSF" by $h_\lambda^c\left(\delta_u;\delta_d,D_{\phi_r}\right)$ instead of $h_\lambda^c\left(\delta_u,\delta_d,D_{\phi_r}\right)$ to underline the fact that δ_d and D_{ϕ_r} are assumed to be known.

An advantage of our approach is that these assumptions can evolve. The formalism will allow to refine our method if we finally decide to estimate either the downstream aberrations or the residual turbulent aberrations. Thus, we can increase little-by-little the complexity of the problem in anticipation of using real data from SPHERE or from another instrument.

4. Joint estimation of wavefront and object algorithm and minimization strategy

This section introduces the criterion to be minimized (4.1) and describes the minimization algorithm, stressing the two stages which constitute its core (4.2 and 4.3). One of these stages presents some convergence difficulties (4.3). The minimization strategy is described as well as some first regularization elements which have been used to constrain the problem for the present validations. One part of the choice is based on physical fundaments, another is based on some minimization criterion constraints. These choices may evolve according to the astrophysical or instrumental cases we consider.

4.1. Definition of the criterion to be minimized and joint estimation

Following the Bayesian inverse problem approach, solving the inverse problem consists in finding the unknowns, firstly the object characteristics $o(\alpha,\lambda)=\{o_\lambda(\alpha)\}_\lambda$, secondly the parameters of the speckle field $h^c_\lambda(\delta_u;\delta_d,D_{\phi_r})$ and $f^*(\lambda)=\left\{f^*_\lambda\right\}_\lambda$, which are the most likely given the data and our prior information about the unknowns. This boils down to minimizing the following criterion:

$$\begin{aligned} & J(o,f^*,\delta_u) \\ = & \sum_\lambda\sum_\alpha \frac{1}{2\sigma^2_{n,\lambda}(\alpha)}|i_\lambda - f^*_\lambda\cdot h^c_\lambda(\delta_u;\delta_d,D_{\phi_r}) - o_\lambda \star h^{nc}_\lambda(\delta_u;\delta_d,D_{\phi_r})|^2(\alpha) \\ & +R_o+R_{f^*}+R_\delta+\cdots. \end{aligned} \tag{4}$$

This criterion is the sum of two terms: the data fidelity term, which measures the distance between the data and the imaging model, and a non-exhaustive list of regularization terms on our unknowns R_o, R_{f^*}, R_δ. The noise variance is assumed to be known beforehand and could be estimated as $\hat{\sigma}^2_{n,\lambda}=\hat{\sigma}^2_{ph,\lambda}+\hat{\sigma}^2_{det,\lambda}$ [25] where $\hat{\sigma}^2_{ph,\lambda}=\max(i_\lambda,0)$ is the photon noise variance and $\hat{\sigma}^2_{det,\lambda}$ is the detector noise variance previously calibrated.

The star flux at each wavelength can be analytically estimated from the criterion provided the regularization on flux is quadratic or absent. In the latter case, the likelihood maximum solution being given by $\frac{\partial J}{\partial f^*_\lambda}=0$, we get:

$$\hat{f}^*_\lambda(o_\lambda,\delta_u)=\frac{\sum_\alpha\left[h^c_\lambda\left(o_\lambda\star h^{nc}_\lambda-i_\lambda\right)/\sigma^2_{n,\lambda}\right](\alpha)}{\sum_\alpha\left[\left(h^c_\lambda\right)^2/\sigma^2_{n,\lambda}\right](\alpha)} \tag{5}$$

Thanks to this analytical expression, the criterion to be minimized is the one of Eq. (4) with f^*_λ replaced by $\hat{f}^*_\lambda$, which will be denoted by $J'(o,\delta_u)$ and depends explicitly on o_λ and δ_u only.

The structure of the criterion of Eq. (4) prompted us to adopt a joint estimation of wavefront and object with an iterative algorithm, which alternates between estimation of the aberrations, assuming that the object is known (multispectral *phase retrieval*) and estimation of the object assuming that the aberrations are known (*non-myopic multispectral deconvolution*). As in these two estimations the same criterion (cf. Eq. (4)) is minimized, the algorithm converges.

4.2. Non-myopic multispectral deconvolution

The *non-myopic multispectral deconvolution* is relatively well-known. The chosen regularization leads to a convex criterion [25] and thus to a unique solution for a given set of aberrations.

The regularization term R_o includes prior spatial and spectral information we have on the object. We chose here a L1-L2 white spatial regularization which assumes the independence between the pixels [26] because we are mainly looking for point sources. The spectral prior is based on the object spectrum smoothness. We currently assume that the object is white (constant spectrum) but as the final aim is to extract some spectra, for future validations we will use a L2 correlated spectral regularization [27] which will involve at each pixel the differences between the spectrum at neighboring wavelengths and will enforce smoothness on the object spectrum.

Even if the *non-myopic multispectral deconvolution* presents a convex criterion which assures a relatively simple minimization, a classical difficulty lies in the two hyperparameters adjustment of the chosen L1-L2 regularization. A first hyperparameter, sets the link between the L1 regularization and the L2 regularization. A second hyperparameter drives the penalization strength. The noise level in the estimated object map depends on the chosen hyperparameters.

A direct consequence is that the performance of the algorithm about the planet flux estimation will be affected by the hyperparameters choice. As the first aim of this work is to detect a planet, we chose the set of hyperparameters which favours the faintest planet we can detect: with a contrast of 10^6. But we have to keep in mind that the estimation flux error will be more important for planets with another contrast and that it would be in the prospects to improve the hyperparameters adjustment. In this paper, we compare the rms values of the differences between the simulated and estimated object images in the focal plane. Thus, the instrument response acts as a low-pass filter and allows to avoid the regularization difficulties.

4.3. Phase retrieval: dealing with local minima

In the *phase retrieval* stage, the number of parameters to estimate in order to rebuild the aberrations is very large, typically 10^3 (see Section 4.3.1). This, combined with the fact that the criterion is highly non-convex, complicates the problem. To get around local minima, several clever numerical solutions resulting from imaging understanding are necessary and described hereafter.

4.3.1. Phase parametrization and regularization

Concerning the phase, we choose the basis of the pixel indicator functions rather than, e.g., a truncated basis of Zernike polynomials, in order to model and reconstruct phases with a high spatial frequency content. Because of the potentially large number of phase unknowns (about 10^3 in our case) we could regularize the phase estimation. To this aim, we could use a functional R_δ proposed specifically for such a phase basis in Refs. [28] and [29].

4.3.2. Choice of an appropriate starting point: very small random phase

In order to keep the computation time reasonable, we use a local descent algorithm to minimize the criterion. Because the latter is highly non-convex, the chosen starting point can lead or not to the global minimum of the criterion. The solution is brought by assuming that the upstream aberrations are small enough at the starting point so that we are fully in the conditions where the Taylor expansion developed in 3.2.1 is valid and where the criterion is less non-convex. It allows the algorithm to avoid many wrong directions, and thus many local minima. As the algorithm converges, the upstream aberration rms value increase towards their true value and a gradual non-linearity of the model is little by little introduced.

For aberrations with very small rms values, the "coronagraphic PSF" h_λ^c is close to zero according to Eq. (12) and thus the analytical flux estimate given by Eq. (4) can diverge. It is then essential to regularize the flux estimation to constrain it to some more physical values and avoid any division by zero. The idea is to use prior information on the star flux. In order to get an analytical solution to our problem, we want a criterion that is quadratic in flux. We thus choose a Gaussian prior law for the flux, leading to the following regularization term:

$$R_{f^*} = \frac{\left(f_\lambda^* - f_0\right)^2}{2\sigma_{f,\lambda}^2} \tag{6}$$

with f_0 being the prior mean flux and $\sigma_{f,\lambda}$ being the prior standard deviation of the flux. It measures the prior knowledge we have on the star flux. This leads to the following expression for the analytic star flux:

$$\hat{f}_\lambda^* = \frac{f_0/\sigma_{f,\lambda}^2 + \sum_\alpha h_\lambda^c \left(i_\lambda - o_\lambda \star h_\lambda^{nc}\right)/\sigma_{n,\lambda}^2}{\sum_\alpha \left(h_\lambda^c\right)^2/\sigma_{n,\lambda}^2 + 1/\sigma_{f,\lambda}^2}. \tag{7}$$

In practice, we choose a very large standard deviation $\sigma_{f,\lambda} = 100 \times \sum_\alpha i_\lambda$, in order not to bias the flux. With such standard deviation, we can choose any mean flux, for example, $f_0 = 0$. This is sufficient to avoid the division by zero in the flux computation and thus the flux divergence.

We test the phase retrieval capability of our algorithm with respect to the chosen starting point, assuming that there is no object to estimate. The minimization results use an additional trick that will be explained in 4.3.3. Three different starting points are studied. For each of them, we give the rms value of the estimated upstream aberration map and the rms value of the difference between the simulated and the estimated maps estimated as follows:

$$\mathrm{rms}^{\mathrm{diff}} = \frac{\left[\sum_\rho \left(\delta_u^{\mathrm{simulated}} - \delta_u^{\mathrm{estimated}}\right)^2\right]^{1/2}}{\left[\sum_\rho \left(\delta_u^{\mathrm{simulated}}\right)^2\right]^{1/2}} \times 100. \tag{8}$$

The inversion is performed with one spectral channel and with a regularization on the star flux estimation. Figure 4 compares some estimated upstream aberration maps (a, b, c) to the simulated one ("true"):

(a) One could think that using a random aberration map with the same rms value as the true aberrations (30 nm at 950 nm) as a starting point would help one find the global minimum. In fact, it does not help because the algorithm converges very fast towards a local minimum and the estimated aberration map ($\mathrm{rms}^{\mathrm{a}} = 307$ nm at 950 nm) is completely different from the simulated one ($\mathrm{rms}^{\mathrm{diff,a}} = 10^3\%$).

(b) Using a zero aberration map as a starting point does not work either. It is probably due to the fact that the approximate model is an even function. For this particularly starting point, the gradient is null which leads to some convergence difficulties. The rms of the difference between the two maps is about $1.4 \times 10^4\%$. The estimated aberration pattern ($\mathrm{rms}^{\mathrm{b}} = 4069$ nm at 950 nm) seems to show that the algorithm does not explore the high frequencies.

(c) The solution we propose is to use as a starting point for the minimization a non-null random aberration map with a small rms value compared to those of the "true" simulated aberration map. In practice, we choose a rms value about 10^8 times smaller than the 'true" value. This leads to a correct estimation of the aberration map ($\mathrm{rms}^{\mathrm{c}} = 30.2$ nm at 95 nm) with a rms of the difference between the two maps of about 0.6%.

If we plot the same results for images simulated with turbulence, the convergence is easier as the presence of turbulence aberrations constrains the problem. The rms of the difference between the estimated aberrations and the simulated aberrations are about $1.8 \times 10^2\%$ ($\mathrm{rms}^{\mathrm{a'}} = 30.7$ nm at 95 nm) , 17% ($\mathrm{rms}^{\mathrm{b'}} = 30.1$ nm at 95 nm) and 17% ($\mathrm{rms}^{\mathrm{c'}} = 30.1$ nm at 95 nm) for the cases (a'), (b') and (c') respectively.

Choosing an aberration map with a small rms value as a starting point of the *phase retrieval* allows us to avoid some local minima by linearizing the highly non-convex model used in the inversion.

4.3.3. Avoiding some local minima by testing quasi-equivalent starting points

In the approximate model, four different aberration maps can give the same image (cf. Equation(14) in Appendix). This means that, from a given starting point, the minimization algorithm can take four different but equivalent directions from the approximate model point of view. But from the point of view of the model used in the inversion (3.2.2), it is not the case because it depends on downstream aberrations, which break the symmetry.

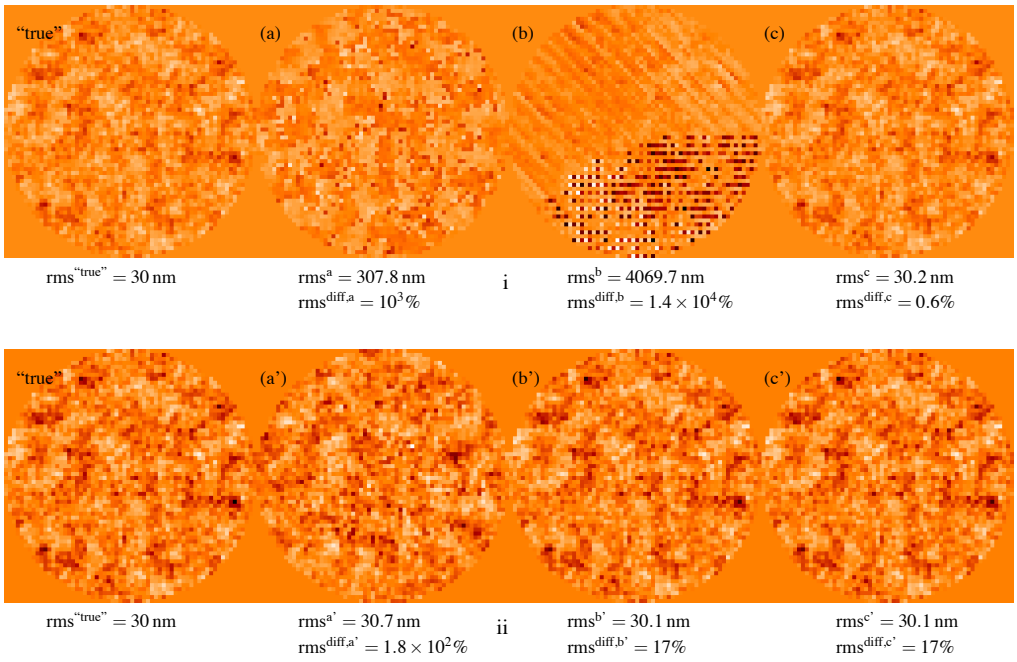

Fig. 4. Choice of an appropriate starting point. Estimated upstream aberration maps with one spectral channel for three different starting points. [Top] Without turbulent aberrations in the simulated images. [Bottom] With turbulent aberrations in the simulated images. From left to right, with a dynamic adapted to the visualization: "true" simulated aberration map, (a) and (a') estimated aberrations with a random aberration map (rms value of the simulated aberrations) as starting point, (b) and (b') estimated aberrations with a zero aberration map as starting point and (c) and (c') estimated aberrations with a random aberration map (rms value 10^8 times smaller than the "true" one) as starting point. The estimation is performed with a regularization on the star flux.

Consequently, a good solution from the point of view of the approximate model may be a not-so-good one from the model used in the inversion point of view. The idea is then to perform an initialization step where the very small random phase is taken as a starting point. A first *phase retrieval* stage is performed with this starting point, leading to a first estimated aberration map denoted by ${\delta_u}^{init,1}(\rho)$. Then, the three other quasi-equivalent aberration maps ${\delta_u}^{init,1}(-\rho)$, $-{\delta_u}^{init,1}(\rho)$ and $-{\delta_u}^{init,1}(-\rho)$ are taken as starting points for three other *phase retrieval* stages. This leads to three more estimated aberration maps denoted by ${\delta_u}^{init,2}$, ${\delta_u}^{init,3}$ and ${\delta_u}^{init,4}$.

Figure (5) shows the four estimated aberration maps at the end of the initialization step. These estimated aberration maps are compared to the simulated one (Fig. (4.d)). The final aberration map chosen as a starting point for the alternating algorithm is the one that gives the minimum value for criterion J of Equation 4:

$$(\delta_u)_{init} = \arg\min \left\{ J\left[\delta_u^{init,1}\right], J\left[\delta_u^{init,2}\right], J\left[\delta_u^{init,3}\right], J\left[\delta_u^{init,4}\right] \right\} \tag{9}$$

It turns out that the chosen set of aberrations is also the one with the closest rms value ($\text{rms}^{b'} = 30.1$ nm at 950 nm) with respect to the 'true" phase (Fig. (4i. "true") and Fig. (4ii. "true")).

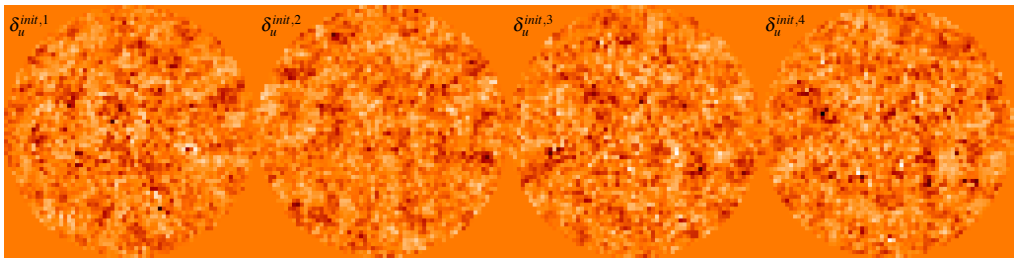

Fig. 5. Estimated upstream aberrations for the four quasi-equivalent aberration maps as starting points. From left to right, with the same dynamic: $\delta_u^{init,1}$, $\delta_u^{init,2}$, $\delta_u^{init,3}$, $\delta_u^{init,4}$. The image simulation is performed with one spectral channel in the presence of turbulent aberrations.

4.3.4. Avoiding some local minima in the multispectral inversions by taking the previously estimated aberration map as starting point

In spite of setting up solutions in order to avoid the local minima while the minimization criterion, we sometimes observe some minimization difficulties in the case of inversions with more than two spectral channels. The reason of this problem has not been identified. That is why we begin to do an inversion with one spectral channel. Then, we add one spectral channel for a two-spectral channel inversion and we take the previous estimated aberration map as a starting point. Doing this when adding some more spectral channels is a way of constraining the problem, waiting for understanding the reason of these minimization difficulties.

4.4. Summary of the developed algorithm

Figure (5) summarizes the different steps of the developed algorithm. The choice of a very small random phase as a starting point is essential because it avoids falling into some local minima (section 4.3.2). An initialization phase is performed, testing the algorithm convergence for the four quasi-equivalent solutions (section 4.3.3). The solution which leads to the smallest criterion value is selected. Then, the minimization core is performed, alternating between the aberration estimation, assuming that the object is known (multispectral *phase retrieval*, section 4.3), and the object estimation, assuming that the aberrations are known (*non-myopic multispectral deconvolution*, section 4.2). Several iterations are performed until the stopping rule of the algorithm is verified. The chosen optimizer is the Variable Metric with Limited Memory and Bounds (VMLM-B) [30].

5. Validation of the inversion method by simulations

In this section, we validate the exoplanet detection capabilities of our inversion method. After giving the numerical simulation conditions, we investigate the estimation quality of the aberrations and the object as a function of the number of images at different wavelengths used. Then, we study the algorithm robustness with respect to the bandwidth and with respect to an error in the calibration of the downstream aberrations, which is assumed to be performed before the data acquisition.

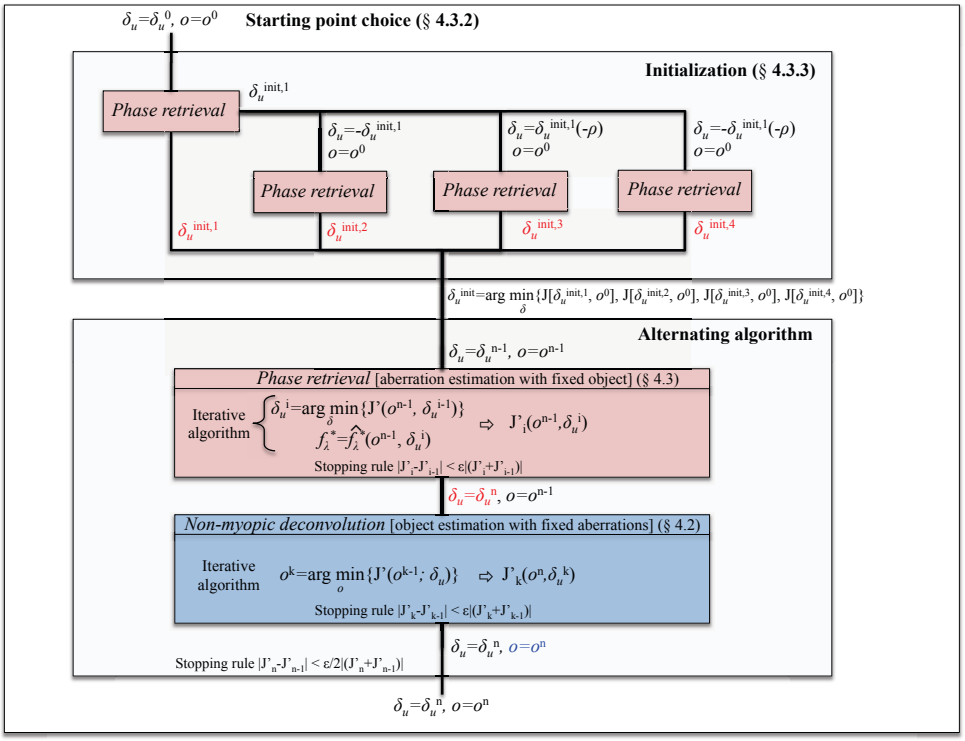

Fig. 6. Block diagram of the algorithm used for the jointly estimation of the object map and static upstream aberrations.

5.1. Test case

5.1.1. Simulation hypothesis

From a data cube of six images simulated with the image formation model of equation (1) and the Sauvage et al. [19] analytical expression of coronagraphic imaging, we jointly estimate the speckle field and the object map. The hypothesis are typical of a SPHERE-like instrument: upstream δ_u and downstream δ_d aberrations respectively simulated with standard deviation of 30 nm and 97 nm, star-planet angular separations of 0.2 and 0.4 arcsec, contrasts, i.e. ratio of star flux over planet flux of 10^5, 10^6 and 10^7, a [950 nm ; 1647 nm] spectral bandwidth and a maximum flux per pixel of 10^8 on the data cube in presence of photon noise corresponding to the observation of a 6-magnitude star for 30 minutes with the VLT. We use 128×128 pixels to simulate our images, shannon-sampled at 950 nm. Thus, the number of unknowns to estimate for the aberration map is about 3×10^3. If we add the unknowns to estimate for the object map, which is about 1.96×10^4, the total number of unknowns is about 2×10^4. Figure (7) shows the simulated objet map (7a) and the associated image in the focal plane (7b). For an easier visualization, we represent the images in the focal plane and not the object map in the following. Figure 7 shows the simulated aberration map (7d) and the associated image of the speckle field in the focal plane (7d).

In the following, we focus on the middle region defined in Figure (7a). Materialized by the

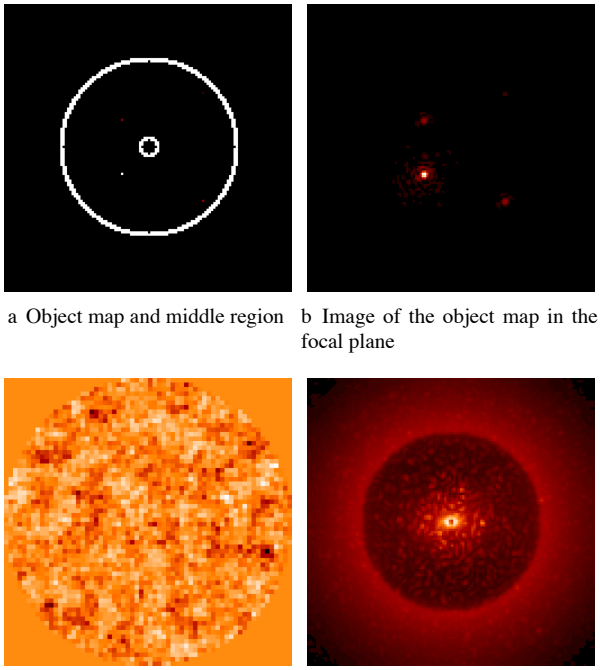

a Object map and middle region

b Image of the object map in the focal plane

c Aberration map

d Image of the speckle field in the focal plane

Fig. 7. Simulated images at $\lambda = 950$ nm. (a) Simulated object map and (b) associated image in the focal plane. The image is obtained by convolving the object map o_λ by the non-coronagraphic psf h_λ^{nc}. (c) Simulated aberrations and (d) associated image of the speckle field in the image focal plane. The image is given by the "coronagraphic PSF" h_λ^c.

two white circles, this is a ring from 2 to 20 λ/D which corresponds to angular distances between $\simeq 0,05$" and $\simeq 0,5$" at 950 nm. In this region, the adaptive optics compensates for the turbulent aberrations. Quasi-static aberrations are dominant, thus they limit the detection. For this reason, this is the region which interests us the most to study the convergence capabilities of our algorithm. We do not expect to detect some planets in the central region inside a disk of 2 λ/D-radius principally because of the high residual starlight. The cut frequency of the adaptive optics being for 20 λ/D, the turbulent aberrations limit the detection in the outer region.

5.1.2. Data processing with "SDI"

We process the simulated images with an optimized "SDI" in order to have a comparison point to estimate the performance of our method. We compare quantitatively the stellar residuals which will limit the detection capability, after post-processing. To do this, we consider the two following bandwidths: [950 nm ; 1650 nm] and [950 nm ; 1150 nm]. The first bandwidth is typical of an IFS-SPHERE-like instrument but this spectral separation is not favorable to the SDI. The second bandwidth is closer to separations we have when using differential filters. For each bandwidth, we take the images at the minimum and maximum wavelengths and we rescale the image at 950 nm with respect to the images at 1150 nm and 1650 nm. Finally, we perform the following spectral differences between the two images (cf. respectively Fig. (8b)

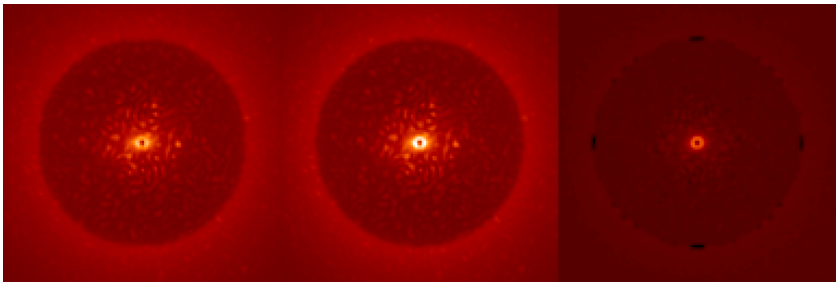

a On the same dynamic: (left) rescaled image at 950 nm multiplied by the γ coefficient, image at 1150 nm (center) before and (right) after speckle subtraction.

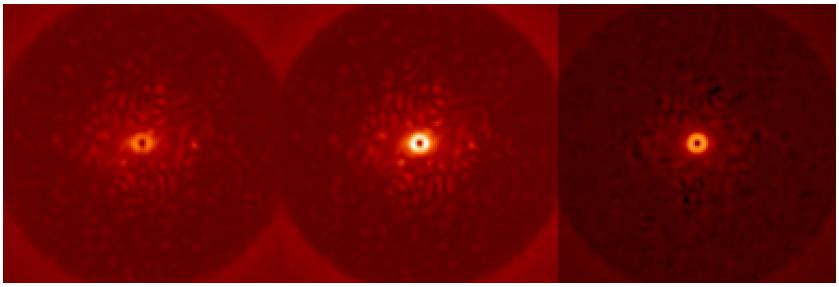

b On the same dynamic: (left) rescaled image at 950 nm multiplied by the γ coefficient, image at 1650 nm (center) before and (right) after speckle subtraction.

Fig. 8. Test case. Speckle field subtractions with the optimized SDI method for two different bandwitdhs.

and Fig. (8a)):

$$i_{\mathrm{diff}_{1650}} = i_{1650\,\mathrm{nm}} - \gamma i_{950\,\mathrm{nm}} \text{ and } i_{\mathrm{diff}_{1150}} = i_{1150\,\mathrm{nm}} - \gamma i_{950\,\mathrm{nm}}, \tag{10}$$

where γ is a coefficient which minimize the squared difference $|i_{\mathrm{max}} - \gamma i_{\mathrm{min}}|^2$ on the middle region $m(\rho)$ defined in Section 5.1.1. γ is the coefficient that minimized the squared difference on this region and is given by [31, 32]:

$$\gamma = \frac{\sum_\rho m(\rho) i_{950\,\mathrm{nm}}(\rho) i_{1650\,\mathrm{nm}}(\rho)}{\sum_\rho m(\rho) i^2_{1650\,\mathrm{nm}}(\rho)}, \tag{11}$$

where m is a mask that is equal to 1 on the pixels belonging to the middle region and 0 elsewhere. This two-channel subtraction reduces the level of stellar halo by a factor 10 (resp 4) in the middle region for the bandwidth [950 nm ; 1150 nm] (respectively [950 nm ; 1650 nm]).

5.2. Inversion with only one spectral channel

We jointly estimate the upstream quasi-static aberration map and the object map with only one spectral channel at 950 nm. Figure (9a) compares the residual speckles in the focal plane after post-processing with the "optimized" SDI method and our method, with respect to the image before post-processing. The inversion with only one spectral channel allows a 81-fold gain to the speckle subtraction, in the middle region defined in Figure (7a). Figure (9b) compares the estimated object image in the focal plane (right) to the simulated one (left). Even if many residuals from the turbulent halo and residual speckles subsist on the object image, one of the planets, that with a contrast of 10^5, is detected at the right position.

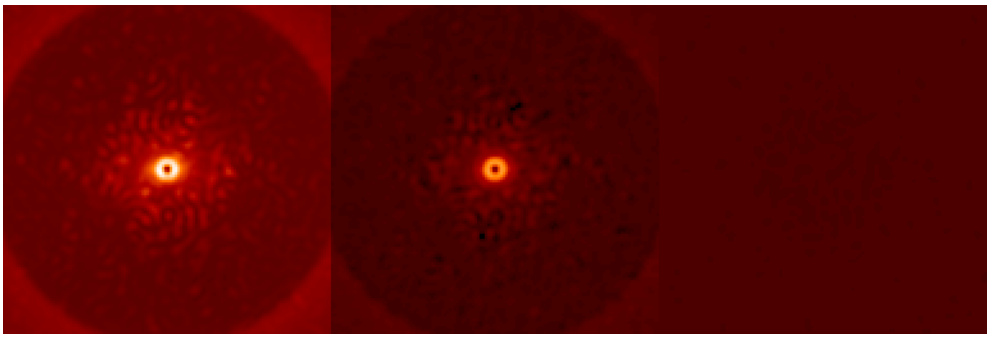

a **Speckle fields.** With the same dynamic, at 1650 nm: (left) image before post-processing and speckle residuals after post-processing with (middle) SDI and with (left) a one-spectral channel inversion. For visualization reasons, the last image was rescaled from 950 nm to 1650 nm.

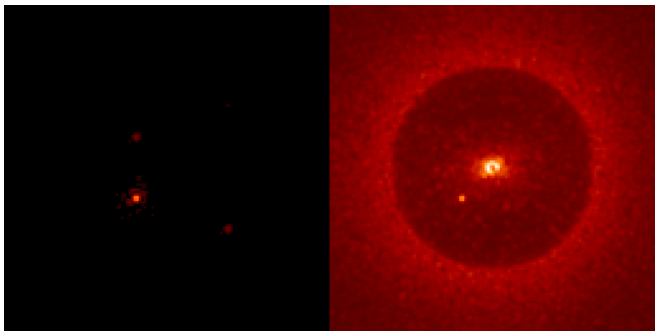

b **Images of object.** With the same dynamic, at 950 nm: (left) simulated and (right) estimated planet image $\left[o_\lambda \star h_\lambda^{nc}\right](x,y)$ with a one-spectral channel inversion.

Fig. 9. Inversion with one spectral channel.

This result shows our algorithm convergence capability in spite of the degeneracy difficulties and the presence of local minima. Actually, it can be surprising to succeed in detecting one planet with a one-spectral channel inversion. Indeed, there is no wavelength diversity to help disentangle the planet from the speckle field. Nevertheless, this can be explained by the symmetry of the speckle field in the coronagraphic imaging for small phases. Boccaletti et al. show that it is a centrosymmetric function [33]. Thus, because the object map we use in our simulation is not centrosymmetric, it is impossible for a planet to be mistaken for a speckle. For the coronagraphic imaging model used, it is only true at first order but it is sufficient to detect the planet with a contrast of 10^5.

5.3. Inversion with multispectral data cubes

We jointly estimate the upstream quasi-static aberration map and the object map with multispectral data. The inversion is realized with two, three, four, five and six spectral channels taken in the simulated data cube of six images. Figure (10a) shows the difference between the simulated and estimated aberration maps for two different inversions. With only one image, some low frequency residuals are visible whereas they have disappeared with a data cube of two images. The aberration map estimation is better with two spectral channels than with only one spectral channel. This demonstrates the multispectral inversion efficiency for the *phase*

retrieval difficult problem.

The speckle field estimation in the focal plane is then improved with the multispectral inversion as shown in Figure (10b). The right image is the subtraction between the simulated speckle field and the estimated one, the former being the result of the inversion with two spectral channels. The inversion with two spectral channels allows a gain of a factor 2000 in the speckle subtraction in the middle region defined in Figure (7a).

Less residuals of upstream aberrations in the object image lead to a better estimation of the object map. Figure (10c) compares the estimated object image for inversions with one (left) and two (right) spectral channels. With two spectral channels, the two planets with a contrast of 10^6 are detected at the right position, in addition to the planet with a contrast of 10^5. The planet with a contrast of 10^7 is not detected because it is flooded by the photon noise. The turbulent halo residuals in the final image, very strong with the one-image inversion, are attenuated by using more images for the inversion. The results with more spectral channels than two are not represented here because they lead to the same visual aspects as those with two spectral channels.

The evolution of the rms value of the difference between the simulated and the estimated speckle fields is represented in Figure (12a), for all the images, in the middle region defined in Figure (7a). In the same way, the evolution of the rms value of the difference between the simulated and the estimated object images is represented in Figure (12b). The rms value of the difference between the simulated and the estimated images decreases with the number of wavelengths used for the inversion. This confirms that adding some more wavelengths, thus more information, improves the joint estimation performance.

5.4. Algorithm robustness study

5.4.1. Bandwidth effect

We study here the bandwidth effect on the image object estimation quality. We take three different bandwidths: from 950 nm to 1650 nm, from 950 nm to 1350 nm and from 950 nm to 1150 nm. The two first bandwidths correspond to operational modes of the SPHERE-IFS instrument whereas the last bandwidth is produced for compromise purposes, more representative of dual spectral separations as used in Dual-Band Imaging.

Figure (12) shows the evolution of the rms value of the difference between the simulated and the estimated speckle fields and object images as a function of the number of wavelengths used in the inversion for the three different bandwidths, in the middle region defined in Figure (7a). The quality of estimation increases with the bandwidth because we add some information for the reconstruction. One can note that the plots decrease and then increase for the two smaller bandwidths. We do not know for sure at the moment if it is a photon noise effect or some other minimization difficulty.

5.4.2. Effect of a calibration error on the downstream aberrations

The previous results were obtained by assuming that the static downstream aberrations are calibrated and perfectly known (cf. section 3.2.1). We study here the effect of calibration errors on this parameter. The downstream aberrations effect is lower and furthermore, in foreseen system, they are expected to be much more stable and easier to calibrate than upstream aberrations. They will be theoretically stable one-day long that means that they will be calibrated by day. Thus, two errors can intervene: the mis-calibration errors and the fact that nevertheless, they can evolve since the calibration. This two kind of errors are simulated by a gaussian noise of 1%, 3%, 5% and 10% of the simulated downstream aberrations which corresponds to adding a random map of 1, 3, 5 and 10 nm-standard deviation to the downstream aberrations one. The inversion is done for data cubes of one, two, three, four, five and six images.

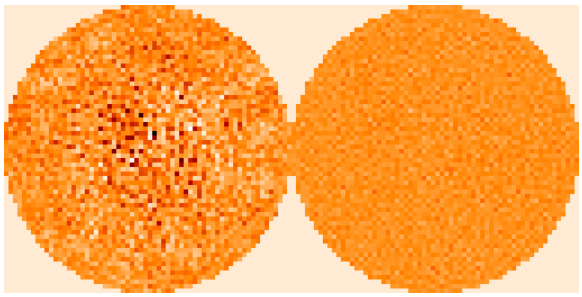

a **Aberration maps.** Difference between the simulated and estimated aberration maps in an inversion with (left) one spectral channel and (right) two spectral channels with the same dynamic.

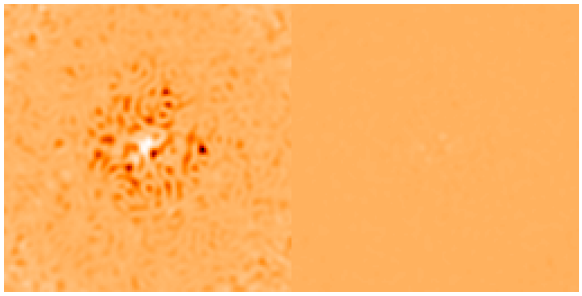

b **Speckle fields.** Speckle residuals after post-processing, with the same dynamic: (left) inversion with one spectral channel and (right) two spectral channels.

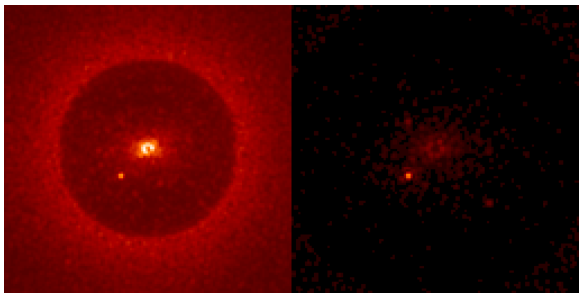

c **Images of object.** Simulated (left) and estimated planets images $\left[o_\lambda \star h_\lambda^{nc}\right](x,y)$, at 950 nm with the same dynamic: (middle) inversion with one spectral channel and (right) two spectral channels.

Fig. 10. Inversion with multispectral data cubes.

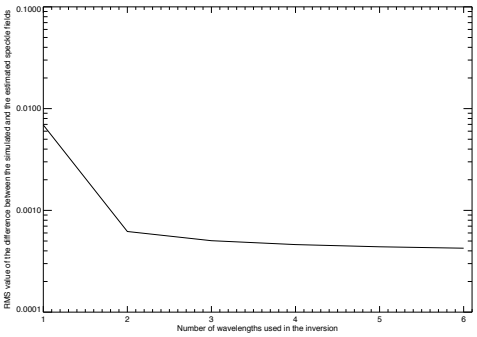

a **Speckle fields.** Difference between the simulated and estimated speckle fields.

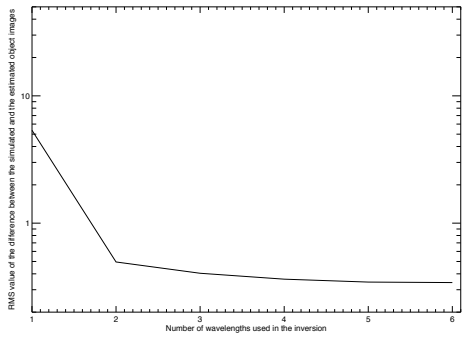

b **Images of object.** Difference between the simulated and estimated object images.

Fig. 11. Inversion with multispectral data cubes. Evolution of the rms value of the difference between the simulated and the estimated images as a function of the number of spectral channels used in the inversion, in the middle region defined in Figure (7a).

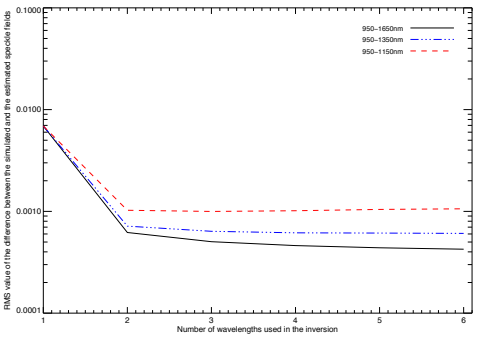

a **Speckle fields.** Difference between the simulated and estimated speckle fields.

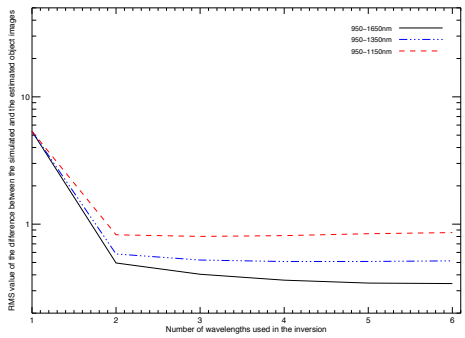

b **Images of object.** Difference between the simulated and estimated object images.

Fig. 12. Bandwidth effect. Evolution of the rms value of the difference between the simulated and the estimated images as a function of the number of spectral channels used in the inversion, in the middle region defined in Figure (7a), for three different bandwidths: from 950 to 1150 nm, from 950 nm to 1350 nm and from 950 nm to 1650 nm.

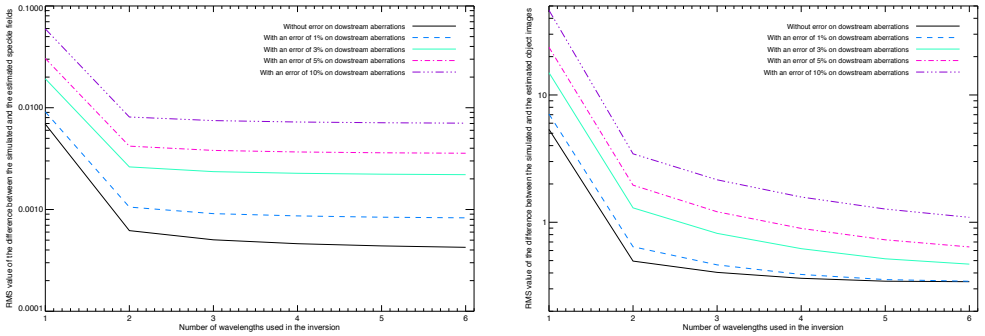

a **Speckle fields.** Difference between the simulated and estimated speckle fields.

b **Images of object.** Difference between the simulated and estimated object images.

Fig. 13. Effect of a calibration error on the downstream aberrations. Evolution of the rms value of the difference between simulated and estimated images as a function of the number of spectral channels used in the inversion, , in the middle region defined in Figure (7a), for different errors on the downstream aberration map.

Figure (13b) shows the evolution of the rms value of the difference between the simulated and the estimated image objects for the different errors on the downstream aberration map, in the middle region defined in Figure (7a). They are compared to the black line which is the plot without error (same as plot for middle region of the Figure (11)). All the inversions benefits from an increase of the spectral channel number. But the most interesting thing is that an increase of the spectral channel number used for the inversion can compensate for a downstream aberration calibration error. For example, with a calibration error of 3%, the inversion with six wavelengths leads to the same rms value between the simulated and the estimated object images of those of the two-wavelength-inversion in the case without error. Moreover, with a calibration error of 1% and a six-wavelength-inversion, it is possible to retrieve the same quality of image reconstruction of the case without error.

6. Conclusion

We have proposed an original method of image restoration for the new generation of planet finders. For the first time, a fine parametric model of coronagraphic imaging, describing the instrument response, is used for the inversion of simulated multispectral images, in a solid statistical framework. The choice of a Bayesian approach allows to use a wide variety of prior information either about the system (aberrations, flux, noise) and about the object of interest. An interest of the method is the possibility of adjusting the weight of the prior information according to the instrumental aberrations and object knowledge and the instrument stability.

In order to set up this method, we have developed an iterative algorithm which estimates jointly the object (*non-myopic multispectral deconvolution*) and the aberrations (*multispectral phase retrieval*). Estimating the aberrations is a difficult issue because of the high non-linearity of the coronagraphic imaging analytical model and the number of unknowns to estimate (about 10^3 in our case). Nevertheless, we have demonstrated the convergence capabilities of the algorithm, by bringing original solutions to the minimization difficulties of the *phase retrieval*.

The restoration of images simulated with a perfect coronagraph is very encouraging for the extraction of planetary signals at levels beginning to be astrophysically interesting. We have demonstrated the efficiency of the method even with only one spectral channel, by achieving a

contrast of 10^5 at 0.2 arcsec. Multispectral redundancy improves the detection as soon as we add one more spectral channel, allowing to achieve a contrast of 10^6 at 0.2 arcsec.

The number of wavelengths used for the inversion seems to be all the more important as the prior information we have on the system is imperfect. We thus believe that multispectral approach will be determining when we confront it with experimental data. This deserves to be studied, as well as how the performance will evolve in the different cases of images simulated with a non-perfect coronagraph, real images from the SPHERE instrument on lab or real images from an instrument on-sky.

Eventually, this method could be used to improve the performance of the existing multispectral imaging instruments, providing some better astrophysical exploitations. We have now demonstrated that we could manage the difficulties linked to the criterion minimization achieving a better contrast than in other approaches. Thus, the method is limited by the analytical imaging model relevancy and the quality of the used prior information. Nevertheless, the current and future instrument specifications have begun to be so severe that we need more and more knowledge of the instrument, particularly for the calibration procedures. That is why the potential of the method is huge. The lessons drawn by applying the method could also facilitate the approach for the design of future instruments as EPICS for the European Extremely Large Telescope [9], and the definition of their calibration procedures.

Acknowledgements

This research is supported by the “Groupement d’Intérêt Scientifique” PHASE.

Appendix A: Indetermination on the estimated aberrations from an image simulated with our approximate model

We show here that four sets of upstream aberrations give the same image in the case of our approximate model. We re-write the expression hereunder, as a function of $\phi_u = (2\pi/\lambda) \times \delta_u$ and without the variables for more readability:

$$\left[h_\lambda^c\right]^{app} = \left|\widetilde{\mathscr{P}_d} \star \widetilde{\phi_u}\right|^2 + \left|\widetilde{\mathscr{P}_d}\right|^2 \star S_{\phi_r}(\alpha) - \left\langle |P[\phi_r]|^2 \right\rangle_t \cdot \left|\widetilde{\mathscr{P}_d}\right|^2 + o\left(\phi^2\right) \tag{12}$$

We consider here the static term $\left|\widetilde{\mathscr{P}_d} \star \widetilde{\phi_u}\right|^2$ and re-write it under the form of an autocorrelation. For this, let's consider two functions $f = \mathscr{P}_d$ and $g = \delta_u$ of the two variables ρ_x and ρ_y and let's denote $\check{f}(\rho) = f(-\rho) = f(-\rho_x, -\rho_y)$.

By using the definition of the intercorrelation $\Gamma_{fg}(\rho)$ and the correlation $\mathscr{C}_{fg}(\rho)$ of the two functions $f(\rho)$ and $g(\rho)$:

$$\begin{aligned} \Gamma_{fg}(\rho) &= f(\rho) \otimes f(\rho) = \int f^*(\rho') f(\rho' + \rho) \mathrm{d}\rho, \\ \mathscr{C}_{fg}(\rho) &= f(\rho) \star g(\rho) = \int f(\rho') g(\rho - \rho') \mathrm{d}\rho, \end{aligned}$$

and the following properties:

$$\left(\widetilde{f}\right)^* = \widetilde{\check{f}^*} \text{ and } f \star g = f \otimes \check{g}^*,$$

we get:

$$\left|\widetilde{f} \star \widetilde{g}\right|^2 = \widetilde{fg} \cdot (\widetilde{fg})^* = \widetilde{fg} \cdot \widetilde{(\check{fg})^*} = \widetilde{fg \star (\check{fg})^*} = \widetilde{fg \otimes fg} = \widetilde{\Gamma_{fg}}.$$

Thus:

$$\left|\widetilde{\mathscr{P}_d} \star \widetilde{\phi_u}\right|^2 = \widetilde{\Gamma_{(\mathscr{P}_d \cdot \phi_u)}} \tag{13}$$

The following properties of the autocorrelation:

$$\begin{aligned} \Gamma_{f(\rho)} &= \Gamma_{f^*(-\rho)} \\ &\text{and} \\ \Gamma_{-f} &= \Gamma_f, \end{aligned}$$

leads respectively to

$$\left| \begin{array}{lcl} \Gamma_{(\mathscr{P}_d \cdot \delta_u)(\rho)} & = & \Gamma_{(\mathscr{P}_d \cdot \delta_u)(-\rho)} \\ \Gamma_{(\mathscr{P}_d \cdot (-\delta_u))(\rho)} & = & \Gamma_{(\mathscr{P}_d \cdot (-\delta_u))(-\rho)} \end{array} \right.$$

$$\text{and}$$

$$\Gamma_{(\mathscr{P}_d \cdot (-\delta_u))(\rho)} = \Gamma_{(\mathscr{P}_d \cdot \delta_u)(\rho)}.$$

Thus:

$$\Gamma_{(\mathscr{P}_d \cdot \delta_u)(\rho)} = \Gamma_{(\mathscr{P}_d \cdot \delta_u)(-\rho)} = \Gamma_{(\mathscr{P}_d \cdot (-\delta_u))(\rho)} = \Gamma_{(\mathscr{P}_d \cdot (-\delta_u))(-\rho)}, \tag{14}$$

which means that the upstream aberration sets $\delta_u(\rho)$, $\delta_u(-\rho)$, $-\delta_u(\rho)$ and $-\delta_u(-\rho)$ are equivalent with respect to the approximate model, because they give the same image. This is true even in the presence of the turbulent term $\left|\widetilde{\mathscr{P}_d}\right|^2 \star S_{\phi_r}(\alpha) - \left\langle |P[\phi_r]|^2 \right\rangle_t \cdot \left|\widetilde{\mathscr{P}_d}\right|^2$.

Appendix B: Indetermination on the estimated aberrations from an image simulated with the Sauvage et al.'s model

In classical imaging, i.e. "non-coronagraphic imaging", the even part sign of the phase can not be deduced from only one image in the focal plane [28]. In other words, if we denote ϕ_p and ϕ_i, the odd and the even parts of the phase, the two phases: $\phi = \phi_p + \phi_i$ and $\phi' = -\phi_p + \phi_i$ give the same image. In this appendix, we show that it is also the case for the Sauvage et al. expression [19] in coronagraphic imaging, if we assume that the even part sign change for all the phases in presence.

The expression of Sauvage et al. is the following:

$$h_\lambda^c = \langle A_n A_n^* \rangle + \left\langle |(\eta_0)|^2 \right\rangle A_d A_d^* - 2\Re\left\{ \langle \eta_0 A_n^* \rangle A_d \right\} \tag{15}$$

with $A_n(\alpha) = \mathrm{TF}^{-1}\left[\mathscr{P}_d(\rho) e^{j\phi_{tot}(\rho)} \right]$, $A_d(\alpha) = \mathrm{TF}^{-1}\left[\mathscr{P}_d(\rho) e^{j\phi_d(\rho)} \right]$, $\phi_i(\rho) = 2\pi \frac{\delta_i(\rho)}{\lambda}$ and $\phi_{tot}(\rho) = \phi_r(\rho) + \phi_u(\rho) + \phi_d(\rho)$. TF[.] denotes the Fourier Transform. $\left\langle |(\eta_0)|^2 \right\rangle$ represents the mean Strehl ratio during observation, such as:

$$\eta_0(t) = \langle \Psi_0(\rho) | \mathscr{P}_u(\rho) \rangle = \frac{1}{S} \iint_\rho \Psi_0^*(\rho) \mathscr{P}_u(\rho) \mathrm{d}^2\rho = \frac{1}{S^2} \iint_\rho \mathscr{P}_u^2(\rho) e^{-j\phi(\rho,t)} \mathrm{d}^2\rho,$$

with $\phi(\rho,t) = \phi_r(\rho,t) + \phi_u(\rho)$.

The first term of Sauvage et al.'s expression $\langle A_n A_n^* \rangle$ is the classical case of non-coronagraphic PSF, which is well-known [28]. The term $A_n A_n^*$ stays identical whatever the sign of the phase even part.

The second term of Sauvage et al.'s expression is the product of two terms: $\left\langle |(\eta_0)|^2 \right\rangle$ and $A_d A_d^*$. The latter stays identical whatever the sign of the phase even part. We take the following phase: $\phi' = -\phi_p + \phi_i$ and we calculate the corresponding $\eta_0'(t)$, assuming that $\rho'' = \rho'$:

$$\begin{aligned}
\eta_0'(t) &= \frac{1}{S^2} \iint_\rho \mathscr{P}_u^2(\rho) e^{-j\phi'(\rho,t)} \mathrm{d}^2\rho \\
&= \frac{1}{S^2} \iint_\rho \mathscr{P}_u^2(\rho) e^{-j\left[-\phi_p(\rho,t)+\phi_i(\rho,t)\right]} \mathrm{d}^2\rho \\
&= \frac{1}{S^2} \iint_\rho \mathscr{P}_u^2(\rho) e^{j\left[\phi_p(-\rho,t)+\phi_i(-\rho,t)\right]} \mathrm{d}^2\rho \\
&= \frac{1}{S^2} \iint_{\rho''} \mathscr{P}_u^2(\rho'') e^{j\left[\phi_p(\rho'',t)+\phi_i(\rho'',t)\right]} \mathrm{d}^2\rho'' \\
&= \frac{1}{S^2} \iint_{\rho''} \mathscr{P}_u^2(\rho'') e^{j\left[\phi(\rho'',t)\right]} \mathrm{d}^2\rho'' \\
&= \left[\eta_0(t)\right]^*
\end{aligned}$$

$\left\langle |(\eta_0)|^2 \right\rangle = \left\langle |(\eta_0 \cdot \eta_0(t)^*)|^2 \right\rangle$ is then independent of the even part sign of the phase. Thus, the product $\left\langle |(\eta_0)|^2 \right\rangle A_d A_d^*$ is also independent of the even part sign of the phase.

We study now the third term $2\Re\{\langle \eta_0 A_n^* \rangle A_d\}$. Assuming that $\phi_d = (\phi_d)_p + (\phi_d)_i$ and $\phi_d' =$

$-(\phi_d)_p + (\phi_d)_i$:

$$\begin{aligned} A'_d(\alpha) &= \mathrm{TF}^{-1}\left[\mathscr{P}_d(\rho)\, e^{j\phi'_d(\rho)}\right] \\ &= \iint_{\rho'}\left[\mathscr{P}_d(\rho)\, e^{j\left[-(\phi_d)_p(\rho)+(\phi_d)_i(\rho)\right]}\right] e^{-2i\pi(\rho\alpha)}\mathrm{d}^2\rho \\ &= \iint_{\rho'}\left[\mathscr{P}_d(\rho'')\, e^{-j\left[(\phi_d)_p(\rho'')+(\phi_d)_i(\rho'')\right]}\right] e^{2i\pi(\rho''\alpha)}\mathrm{d}^2\rho'' \\ &= [A_d]^* \end{aligned}$$

As well as the previous demonstration we can show that $A_n^* = A_n$. Under the effect of the following transformation: $\phi \to \phi'$, the different terms become:

$$\begin{cases} \eta_0 \to \eta_0^* \\ A_n^* \to A_n \\ A_d \to A_d^* \end{cases}$$

In other words, $\langle \eta_0 A_n^* \rangle A_d \to [\langle \eta_0 A_n^* \rangle A_d]^*$. When we take the conjugate of a complex number, only the sign of the imaginary part change. As we take the real part of this expression, changing the even part of the phase does not change the term.

To conclude, like in classical imaging, changing the even part of the phase sign does not change the image in the focal plane. This means that two sets of aberrations give the same image. But if we assume like in this communication, that the downstream aberrations are fixed and known, this raises the degeneracy.